mining

MDPI

Article

Numerical Investigation of Multifield Coupling in Surrounding Rock of Deep Roadways Under High-Temperature Conditions

Yanzi Lei [1], Yuliang Sun [1,2,*], Jiangbo Li [3], Kaipeng Wang [1,2] and Shaoming Ma [1]

[1] CCTEG Xi'an Research Institute (Group) Co., Ltd., Xi'an 710077, China
[2] Xi'an Coal Science Geothermal Energy Development Co., Ltd., Xi'an 712044, China
[3] School of Energy and Mining Engineering, Xi'an University of Science and Technology, Xi'an 710054, China
* Correspondence: syldrgs@163.com

Abstract

Deep high-temperature excavation faces suffer severe heat and moisture hazards, but coupled transport in surrounding rock and the influence of ventilation and rock properties remain unclear. A coupled heat–moisture–airflow transport model considering moisture diffusion in the surrounding rock was established, and a three-dimensional numerical model was built. The model explicitly resolves the airflow field, the temperature field and the moisture field; stress effects are discussed as a stress-dependent extension rather than a fully solved mechanical field. Sensitivity analysis and response surface methodology were applied. Results show that the air duct jet creates a nonuniform flow that controls temperature and humidity zoning. Near the inlet, temperature drops by more than 20 °C within 1 to 5 days, and after 50 days most of the roadway falls below 35 °C. Relative humidity near the heading face decreases from 0.7 to below 0.6 and later recovers to 0.62 to 0.65. When thermal conductivity increases from 1 to 4 W m^{-1} K^{-1}, the low temperature zone shrinks sharply. When the moisture transport coefficient decreases from 10^{-5} to 10^{-7} m^2/s, relative humidity drops significantly. Response surface analysis shows that initial rock temperature has the greatest influence on average temperature, and the interaction between equipment heat dissipation and spray humidification also has a clear influence. These findings clarify coupled heat and moisture transport in surrounding rock and support heat hazard prediction, ventilation cooling, and humidity control in deep mines.

Keywords: high-temperature excavation face; heat and moisture transport; multifield coupling simulation; rock thermal and moisture properties

Academic Editor: Chaoshui Xu

Received: 13 October 2026
Revised: 16 November 2026
Accepted: 18 November 2026
Published: 20 November 2026

Copyright: © 2026 by the authors. Licensee MDPI, Basel, Switzerland. This article is an open access article distributed under the terms and conditions of the Creative Commons Attribution (CC BY) license.

1. Introduction

As one of the world's major coal-producing countries, China has experienced a progressive transition from shallow to deep mining due to the continuous depletion of shallow mineral resources [1,2]. Over 53% of China's coal reserves are buried at depths exceeding 1000 m, and by the end of 2024, the number of deep mines with mining depths exceeding 800 m had surpassed 100 [1,3,4]. Deep mining is confronted with far more complex geological and geotechnical conditions, including high in situ stresses, high pore pressures, and elevated geothermal gradients [5,6]. Excavation activities severely disturb the original equilibrium, inducing the redistribution and strong coupling of the stress,

seepage, and temperature fields [7]. As mining depth increases, the geothermal gradient leads to a sharp rise in original rock temperature. Intense heat dissipation from the surrounding rock has become the most significant factor leading to heat hazards in deep mines [8,9]. According to incomplete statistics, over 200 coal mines globally face thermal hazard threats [10]. These elevated temperatures not only severely threaten the physiological health and work efficiency of personnel but also pose serious challenges to the reliable operation of precision equipment [11,12]. Therefore, research on the formation mechanisms of thermal environments under high geothermal conditions and heat hazard control technologies has become a critical scientific issue in the field of deep mining [13,14].

The exploration of heat and moisture transport in mines began in the 1980s, with early studies largely based on the assumption of dry surrounding rock, primarily focusing on convective heat transfer between roadway airflow and walls and its analytical solutions [15]. In the 21st century, the large-scale development of deep resources transformed high-geothermal hazards from localized occurrences into a common industry-wide challenge. He et al. [16] conducted systematic theoretical research on deep heat hazard control and developed the HEMS (Heat Hazard Control and Geothermal Extraction System) cooling system, achieving a technological breakthrough in waste heat conversion and utilization under extreme conditions with original rock temperatures exceeding 50 °C [17]. From 2011 to 2020, research focus gradually shifted toward "temperature seepage stress" multi-field coupling mechanisms, with particular emphasis on the feedback relationships among pore water seepage, stress redistribution, and temperature evolution under mining-induced disturbances [18,19].

In recent years, significant advances have been made in understanding the thermal environment of deep mine working faces. Qing et al. [20] investigated the temperature field and heat dissipation evolution of roadway surrounding rock through numerical simulation and similar experiments. A recent study on heat dissipation in high-temperature mine roadways established that rock thermal conductivity is the most critical controlling factor in the long-term stage [21]. Meanwhile, research on the spatiotemporal dynamics of heat hazard formation in high-temperature working faces identified surrounding rock as the dominant heat source, contributing a major proportion of total heat dissipation [22]. Dynamic modeling of airflow temperature fields in advancing deep coal mining faces revealed significant spatiotemporal heterogeneity, with air temperature exhibiting a "slow sharp slow" rise along airflow paths [23]. Field implementation of cooling strategies based on quantitative models achieved an average temperature reduction of 9.5 °C in mining faces [24].

Regarding multi-field coupling, a coupled hydro-thermo-mechanical model based on TLF-SPH has been developed to simulate crack propagation and instability processes in fractured rock masses, successfully simulating the seepage and heat transfer processes of surrounding rock under different coupling conditions [25]. The coupling mechanism between pore water seepage and thermal diffusion was revealed through hydro-thermal coupling simulation, demonstrating that when the direction of heat conduction is opposite to the diffusion direction of seepage, the "temperature carrying effect" of pore water hinders the rate of heat conduction [26]. More recently, a coupled thermo-hydro-mechanical lattice Boltzmann Peridynamic (LBPD) model was proposed to simulate rock mass fracturing processes under multi-physics conditions, effectively capturing dynamic thermal exchange at fracture interfaces and flow disturbances induced by fracture propagation [27]. A comprehensive thermal hydraulic mechanical (THM) coupling numerical model was also developed to investigate stress distribution, deformation mechanisms, and long-term stability of surrounding rock under multi-physical interactions in ultra-deep mine shaft excavations [20]. In addition, a fully coupled heat and mass transfer framework that systematically integrates deep hydrothermal migration with evaporation-

driven heat exchange was proposed to characterize the thermal-moisture transfer and thermal environment spatiotemporal evolution of roadways [28]. Multi-factor orthogonal experimental analysis revealed that surrounding rock temperature has the most dominant impact on ambient temperature, followed by airflow relative humidity, airflow temperature, evaporation factor, ventilation volume, and upwelling water parameters [29].

However, despite these substantial research efforts, the excavation face remains the most severely affected area in terms of mine heat hazards [30]. With increasing mining depth, although ventilation and refrigeration technologies continue to evolve, the strong coupling among the temperature field and seepage field of the surrounding rock under mining-induced disturbances remains the core bottleneck limiting cooling efficiency [31]. Current understanding of the coupled heat moisture transport mechanisms within the surrounding rock of excavation faces remains insufficient, making dynamic prediction and real-time regulation difficult to achieve [32]. In particular, the coupled heat and moisture transport in unsaturated surrounding rock—where temperature gradients drive moisture migration and moisture concentration gradients in turn affect heat transfer—has not been adequately addressed in existing models. Most existing studies treat heat and moisture transport separately or focus on dry surrounding rock conditions, neglecting the latent heat exchange associated with moisture evaporation and the synergistic effects of heat and moisture on the thermal environment. Furthermore, the influence of key physical properties of surrounding rock—such as thermal conductivity and moisture transport coefficient—on the coupled evolution of temperature and humidity fields has not been systematically quantified.

Despite these efforts, most previous studies either treat heat and moisture transport separately, assume dry surrounding rock, or do not resolve the non-uniform airflow produced by the air duct. The latent heat of moisture evaporation and the combined influence of key rock properties on the temperature–humidity field therefore remain insufficiently quantified. This study addresses these gaps in three ways: (i) it establishes a coupled heat–moisture–airflow transport model that includes moisture diffusion and the associated latent heat exchange; (ii) it builds a three-dimensional roadway model that resolves the air-duct jet and its control on temperature and humidity zoning; and (iii) it quantifies the effects of thermal conductivity, moisture transport coefficient and major source terms through sensitivity analysis and response surface methodology.

2. Materials and Methods

2.1. Heat Moisture Transport Process in the Surrounding Rock of High-Temperature Excavation Faces

After excavation and ventilation of underground surrounding rock, the original heat and moisture equilibrium is disrupted due to the temperature and concentration differences existing among the surrounding rock, the thermal (moisture) insulation layer, and the airflow. The continuous migration of heat and moisture across the insulation layer toward the airflow causes cooling and drying within the surrounding rock and the insulation layer. This phenomenon gradually extends from the wall surface into the deep rock mass over time until a new equilibrium is reached. Meanwhile, the roadway airflow, due to convective heat and mass transfer, experiences temperature rise and increased moisture content, exhibiting significant unsteady heat conduction and mass transfer characteristics. The dynamic boundary of this heat and mass loss extending into the deep rock mass is typically defined by the critical range where the temperature and humidity states recover to 99.9% of the original rock level, and this region is referred to as the "heat (and moisture) adjusting zone."

The formation and expansion range of this zone are jointly governed by the thermal (and moisture) physical properties of the surrounding rock, the thickness of the insulation

layer, and its thermal conductivity and mass diffusion coefficient. When the insulation layer is thicker and its thermal conductivity and mass diffusion coefficient are smaller, the transfer rate of heat (and moisture) is reduced, resulting in a slower increase in the radius of the heat-adjusting zone and a smaller final extent. Furthermore, due to convective heat and mass transfer, the temperature (and humidity) difference along the airflow direction gradually diminishes, and consequently, the radius of the heat-adjusting zone in spatial distribution is larger near the air inlet than near the outlet.

Heat conduction and mass diffusion within the deep surrounding rock are in a state of strong mutual coupling. Heat transfer induced by temperature gradients accelerates the mass diffusion process, while moisture transfer driven by moisture concentration gradients is inevitably accompanied by heat diffusion. The greater the moisture gradient, the more intense the mass transfer of water, and the faster the corresponding thermal diffusion, and vice versa. This unsteady heat conduction and mass transfer process, resulting from the interaction between thermal diffusion and mass diffusion, constitutes the core physical mechanism of heat moisture transport in the surrounding rock of high-temperature excavation faces.

2.2. Theoretical Basis of Heat Moisture Transport in Surrounding Rock

In thermodynamic theory, the modes of heat conduction differ among materials in different phases. As a non-conductive solid, the roadway surrounding rock is subject to temperature differences and heat transfer, resulting in temperature variations at different positions within the body, while the temperature at a given position also changes over time. Accordingly, in thermodynamics, the overall temperature distribution at each point within an object at each instant is defined as the temperature field, which is generally a function of time and spatial coordinates, expressed as Equation (1):

$$T = f(x, y, z, \tau) \tag{1}$$

where x, y, z are the spatial coordinates in the Cartesian coordinate system, and τ is the time coordinate.

In the heat transfer process, the amount of heat transferred through a given cross-section per unit time is proportional to the temperature change rate at that cross-section. The direction of heat transfer is from the high-temperature region to the low-temperature region, opposite to the direction of temperature increase. This can be expressed in terms of heat flux density as Equation (2):

$$q = -\lambda \frac{\partial T}{\partial x} \tag{2}$$

where q is the heat flux density, i.e., the heat flow rate per unit cross-sectional area per unit time, in J/(m²·s); λ is the thermal conductivity of the material, in W/(m·°C).

In three-dimensional heat transfer problems, the heat flux density must be specified with its vector direction, expressed as Equation (3):

$$\begin{cases} q = -\lambda gradT \\ gradT = \dfrac{\partial T}{\partial x} i + \dfrac{\partial T}{\partial y} j + \dfrac{\partial T}{\partial z} k \\ q = q_x i + q_y j + q_z k \end{cases} \tag{3}$$

where gradT is the temperature gradient, in °C/m; i, j, k are the unit vectors along the x, y, z axes in the three-dimensional Cartesian coordinate system; and q_x, q_y, q_z are the magnitudes of the heat flux density components along the x, y, z axes, respectively.

According to Fourier's law of heat conduction, we have Equation (4):

$$q_x = -\lambda_1 \frac{\partial T}{\partial x} \quad q_y = -\lambda_2 \frac{\partial T}{\partial y} \quad q_z = -\lambda_3 \frac{\partial T}{\partial z} \tag{4}$$

https://doi.org/10.3390/mining6040110

where λ_1, λ_2, λ_3 are the thermal conductivities of the same conducting body along the x, y, z directions, respectively.

To simplify the solution process for heat dissipation from roadway surrounding rock, the following standardized assumptions are made regarding the heat transfer characteristics and boundary conditions of the surrounding rock:

The roadway surrounding rock is a homogeneous and isotropic medium, with identical thermophysical properties in all directions, and the thermal conductivity λ is a constant.

The airflow in the roadway is in a steady flow state. To illustrate the heat-conduction mechanism and the finite-difference discretization, a local two-dimensional simplification is adopted in this subsection, in which the axial temperature gradient is neglected within a short differential segment. This simplification is used only for the analytical derivation of Equation (5) and does not apply to the three-dimensional numerical model presented in Section 2.4, where the axial temperature variation along the roadway is fully resolved.

The roadway surrounding rock serves only as a carrier for heat transfer within the crust, with no internal heat generation, i.e., the internal volumetric heat source intensity $q_v = 0$. Consequently, the two-dimensional unsteady heat conduction differential equation for the temperature field of the roadway surrounding rock can be derived as Equation (5):

$$\frac{\partial T}{\partial \tau} = a\left(\frac{\partial^2 T}{\partial x^2} + \frac{\partial^2 T}{\partial y^2}\right) \tag{5}$$

where $a=\lambda/(\rho c_p)$ is the thermal diffusivity, λ is the thermal conductivity, ρ is the density, and c_p is the specific heat capacity at constant pressure.

In the three-dimensional numerical model, moisture transport in the surrounding rock is described by the moisture diffusion equation:

$$\frac{\partial \theta}{\partial \tau} = \nabla \cdot (\beta \nabla \theta) + S_m \tag{6}$$

where θ is the volumetric moisture content, β is the effective moisture diffusion coefficient (m^2/s), and S_m is the moisture source/sink term. The energy equation for the surrounding rock includes the latent heat associated with moisture evaporation:

$$\rho c_p \frac{\partial T}{\partial \tau} = \nabla \cdot (\lambda \nabla T) - L_v \dot{m}_{evap} \tag{7}$$

where L_v is the latent heat of vaporization (J/kg) and $\dot{m}_{evap}$ is the evaporation rate ($kg/(m^3 \cdot s)$).

2.3. Definite Conditions

For unsteady heat and mass transfer problems, the definite conditions consist of four aspects: (1) geometric conditions, (2) physical conditions, (3) initial conditions, and (4) boundary conditions.

(1) Geometric conditions

An infinitely long circular roadway, with the thermal (and moisture) insulation layer having an outer radius r and an inner radius.

(2) Physical conditions

The roadway surrounding rock has no internal heat source and no internal moisture source.

(3) Initial conditions

$$T(z,\tau)|_{\tau=0} = T_0 \rho_w(z,\tau)\,|_{\tau=0} = \rho_{w0}$$

(4) Boundary conditions

For the complex boundary conditions at the interface between the static air layer and the boundary layer of the roadway airflow ($r = r_{0-\delta}$), the boundary condition of the third kind can be employed for description. Within a differential segment dz, the variations in airflow temperature and humidity are relatively small. By combining such boundary conditions with the differential equations of mass diffusion and heat conduction, a complete mathematical model describing the heat conduction and mass transfer process in the region near the static fluid layer can be established. Thus, it can be approximately assumed that the variations in airflow temperature and humidity are small, satisfying the model simplification conditions.

(5) Solution verification

Initial conditions:

$$T(z,\tau)|_{\tau=0} = T_0, \rho_w(z,\tau)\ |_{\tau=0} = \rho_{w0} \tag{8}$$

where T_0 is the initial rock temperature, ρ_w is the water (moisture) density in the rock, and ρ_{w0} is its initial value.

The finite difference method is adopted for discretization, yielding:

$$\begin{aligned} T_i^k &= \left(\frac{\Delta\tau\lambda}{\rho c\Delta z^2} - \frac{\rho c v_z}{2\Delta z}\right) T_{i-1}^{k+1} - \frac{C_0 D}{4\Delta z^2} T_{i-1}^{k+1} \rho_{w(i-1)}^{k+1} + \frac{C_0 D}{4\Delta z^2} T_{i-1}^{k+1} \rho_{w(i+1)}^{k+1} \\ &+ \frac{1+2\lambda\Delta\tau}{\rho c\Delta z^2} t_i^{k+1} + \left(\frac{\Delta\tau}{2v_z\Delta z} - \frac{\Delta\tau}{\rho c\Delta z^2}\right) t_{i+1}^{k+1} \end{aligned} \tag{9}$$

After discretizing the initial conditions:

$$T_i^0 = T_0, \rho_{wi}^0 = \rho_{w0} \tag{10}$$

Through the finite difference method, the heat conduction differential Equation (8) is transformed into the algebraic equation system represented by Equation (9). Based on numerical computation programming, the airflow temperature field in the roadway is obtained. The numerical reliability of the discretized model is then evaluated through the mesh-independence analysis presented below.

2.4. Establishment of the Numerical Model for Heat Moisture Transport in the Surrounding Rock of High-Temperature Excavation Faces

To investigate the influence of surrounding rock properties on the temperature and humidity of the excavation face, a corresponding three-dimensional numerical model was established, as seen in Figure 1. The model has a total length of 250 m, with a roadway height of 5 m and width of 3.5 m. An air duct with a square cross-section of 1 m × 1 m is arranged at a height of 2 m above the roadway floor and 0.5 m from the coal wall. In the base scenario used for the surrounding-rock property analysis in Section 3.1, only heat and moisture release from the surrounding rock and ventilation are considered. The single-variable cases in Sections 3.1.4 and 3.1.5 are multiple runs of this base scenario with one parameter changed at a time. Other heat and moisture sources, including equipment heat dissipation, transport heat dissipation, water inflow, personnel heat dissipation and spray humidification, are not included in the base scenario; they are introduced separately in the response-surface scenario in Section 3.2.

The numerical model was discretized using an unstructured tetrahedral mesh generated in COMSOL Multiphysics (Version 6.4). The mesh was refined near the air-duct outlet, the heading face and the roadway wall to resolve the high-velocity jet and the steep temperature and humidity gradients, while a coarser mesh was used in the far-field surrounding rock. Five boundary layers were applied adjacent to the roadway wall. The minimum and maximum element sizes were 0.015 m and 0.35 m, respectively, and the total number of elements was approximately 704,216.

The boundary conditions were set as follows. At the air-duct inlet, a velocity inlet was prescribed with air velocity 15 m/s, temperature 25 °C and relative humidity 0.6. At the roadway outlet, a pressure outlet with zero gauge pressure was applied, and the outflow was assumed to be fully developed. At the roadway wall, conjugate heat and moisture exchange between the airflow and the surrounding rock was represented by third-kind boundary conditions, with the convective heat-transfer coefficient and convective mass-transfer coefficient calculated from the local airflow field. The outer boundary of the surrounding rock was set at the original rock temperature of 55 °C and initial relative humidity of 0.7, far enough from the roadway to avoid boundary effects. The initial temperature and relative humidity of the rock matrix were 55 °C and 0.7, respectively.

The material parameters used in the model are as follows. For the surrounding rock, the density, specific heat capacity and thermal conductivity were 2500 kg/m^3, 1000 J/(kg · K) and 2.5 W/(m · K), respectively, and the moisture transport coefficient was 1×10^{-7} m^2/s. For the air, the density, dynamic viscosity and specific heat capacity were 1.18 kg/m^3, 1.85×10^{-5} Pa · s and 1005 J/(kg · K), respectively. The latent heat of vaporization was 2.26×10^6 J/kg. These parameters were kept constant in the base case, and the effects of thermal conductivity and moisture transport coefficient were examined in the sensitivity analysis.

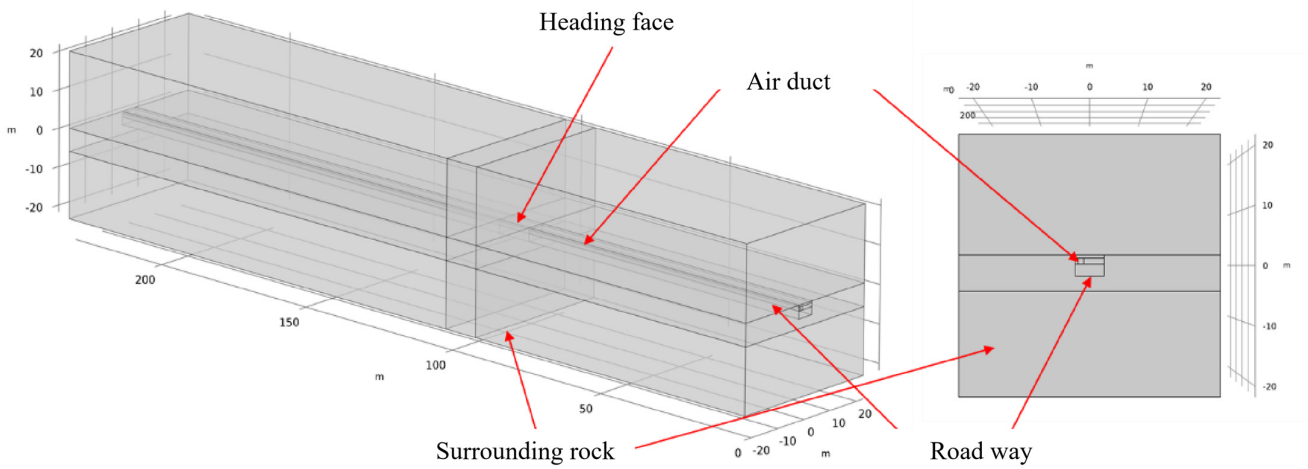

Figure 1. Geometric Schematic Diagram of the Model.

Three meshes with different refinement levels were generated: a coarse mesh (312,480 cells, minimum cell size 0.045 m), a medium mesh (704,216 cells, minimum cell size 0.030 m) and a fine mesh (1,286,540 cells, minimum cell size 0.020 m). The same initial conditions, boundary conditions, time step and solver settings were used for all cases. The outlet average air temperature and relative humidity at 50 d, and the temperature at a monitoring point 50 m from the inlet and 1.5 m above the floor, were selected as comparison indicators.

The coarse mesh deviates from the fine mesh by up to 0.41 °C in temperature and 0.008 in relative humidity. In contrast, the medium mesh deviates from the fine mesh by less than 0.15 °C and 0.003, respectively. Further refinement to the fine mesh does not change the predicted temperature and humidity fields significantly but increases the computation time by a factor of approximately 2.6. Therefore, the medium mesh was selected for all simulations to balance numerical accuracy and computational cost.

The numerical simulations were performed using COMSOL Multiphysics. Given that the ventilation in the roadway involves forced convection with high Reynolds numbers,

the Realizable k − ε turbulence model was employed to capture the turbulent flow characteristics. The transport equations were solved using a fully coupled nonlinear solver based on the Newton-Raphson iteration method.

For the transient heat and moisture transfer process, a Backward Differentiation Formula (BDF) was adopted for time integration. The time step was set as adaptive with an initial step of 10 s and a maximum step of 3600 s, and the relative tolerance was set to 1×10^{-4}.

The convergence criteria for all governing equations were based on the residual error, which was strictly controlled to be below 1×10^{-4} or 10^{-5} at each time step. In addition, to ensure the accuracy of the results, the temperature at the heading face center was tracked to guarantee that the steady-state condition was reached before data extraction.

To ensure the temporal discretization accuracy of the 50-day transient simulation, a time-step independence test was conducted under the adaptive time-stepping scheme. Since the solver automatically adjusts the step size based on error estimates, the maximum allowable time step (Δt_{max}) was selected as the control variable to evaluate time convergence. Three cases were tested: Δt_{max} = 3600 s, 1800 s, and 900 s. As shown in Table 1, the temperature and relative humidity at the roadway outlet at different time nodes (e.g., 1, 10, 25, and 50 days) exhibit negligible differences across the three cases. The maximum relative error is less than 1%. Therefore, to balance computational accuracy and efficiency, the maximum time step of 3600 s was adopted for all subsequent simulations.

Table 1. Comparison of temperature and relative humidity at the roadway outlet under different maximum time steps.

Time (Days)	Temperature (°C)			Relative Humidity		
	Δt_{max} = 3600 s	Δt_{max} = 1800 s	Δt_{max} = 900 s	Δt_{max} = 3600 s	Δt_{max} = 1800 s	Δt_{max} = 900 s
1	33.47	33.46	32.46	0.652	0.652	0.652
10	35.15	35.12	35.12	0.619	0.618	0.618
25	36.48	36.44	36.43	0.604	0.603	0.604
50	37.21	37.17	37.16	0.595	0.595	0.595

Since field measurements were not available for the specific roadway studied here, the reliability of the coupled heat–moisture–airflow model was verified against the validated model and field data reported by Li et al. [33], which shares the same physical coupling framework (non-isothermal airflow, unsteady rock heat conduction, and moisture transfer driven by evaporation) and similar high-temperature roadway conditions. In that study, the simulated airflow temperature and relative humidity profiles along the roadway were shown to agree well with on-site measurements. The close agreement between our simulation trends and those reported in the validated literature confirms that the present model captures the essential coupled transport processes with acceptable engineering accuracy.

3. Results

3.1. Analysis of Simulation Results of Heat Moisture Transport in the Surrounding Rock of the Excavation Face

3.1.1. Airflow Velocity Distribution Characteristics of the Model

Numerical simulation results show that the three-dimensional flow field in the roadway is dominated by the air duct jet. The airflow, with a local maximum velocity of approximately 16 m/s, is discharged from the square air duct with a side length of 1 m, forming a high-speed jet core zone within the confined roadway space. Its axial kinetic energy decays rapidly with downstream distance, and the airflow velocity at the distal end generally drops below 2 m/s, creating a significant velocity gradient.

From the contour distribution of the airflow velocity cloud map in Figure 2, the flow field exhibits spatial asymmetry. On the side near the coal wall, the airflow velocity decays more rapidly due to wall friction and boundary layer effects, whereas along the roadway centerline, a relatively higher velocity of 4 8 m/s is maintained, extending further in the longitudinal direction. This reflects a flow mechanism in which the airflow energy is primarily transported axially while simultaneously dissipating transversely toward the walls.

The uneven airflow velocity distribution directly affects the heat and moisture transfer processes. The intense convection in the air duct outlet region and the axial high-velocity zone significantly enhances the wall heat transfer coefficient, forming efficient transport pathways for heat and water vapor, and accelerating the cooling and drying of the surrounding rock surface. In contrast, in the near-wall regions and the distal end of the roadway, where the airflow velocity is extremely low, heat and moisture exchange is forced to degrade into slow conduction and diffusion processes within the rock mass, which readily leads to the accumulation of energy and moisture and induces localized high-temperature and high-humidity environments. The simulation indicates that the spatial heterogeneity of the velocity field is the core hydrodynamic factor responsible for the non-uniform zonal evolution of temperature and humidity at the excavation face. The airflow velocity distribution of the model is shown in Figure 2.

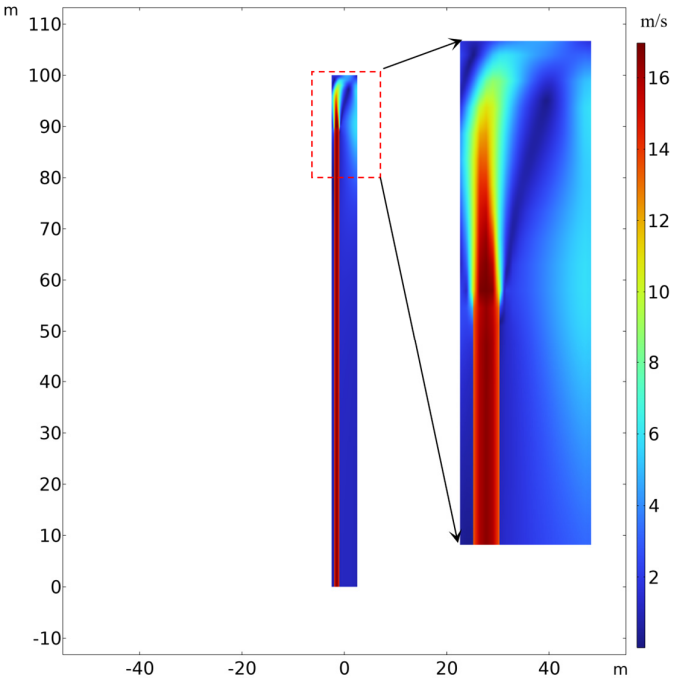

Figure 2. Airflow velocity distribution in the model.

3.1.2. Temperature Variation Characteristics Along the Roadway

Based on the multi-field coupled numerical simulation, the evolution of the roadway temperature field during ventilation exhibits pronounced spatiotemporal dynamic characteristics. At the initial moment (0 d), the system is in a state of thermal equilibrium, with the surrounding rock temperature uniformly at 55 °C, and only a low-temperature zone of approximately 25 °C is formed near the air duct outlet due to the injection of cold air.

Upon the commencement of ventilation, the temperature field responds rapidly. Over time (from 0 d to 30 d), the temperature field enters a conduction-dominated stage. As can be seen from Figure 3, at 50 d, the average air temperature in the first 30 m of the roadway decreased from the initial rock temperature of 55 °C to 27.8–34.6 °C, a reduction

of 20.4–27.2 °C. At 50 m from the air duct, the temperature stabilized at 32.1 °C, which is 22.9 °C lower than the initial rock temperature. The length of the zone with T < 35 °C reached approximately 42 m at 50 d, and the high-temperature zone is compressed toward the heading face. In the range of 0 30 m from the air duct, the temperature drops sharply to 25 30 °C within 1 5 d, representing a temperature reduction of more than 20 °C. Beyond 30 m, the cooling rate slows down, the propagation speed of the thermal influence boundary decelerates, the heat conduction within the surrounding rock intensifies, and the overall cooling rate moderates.

After long-term ventilation (30 d to 50 d), the temperature field approaches a quasi-steady state. Figure 4 show that at 50 d, the temperature in most regions drops below 28 °C, forming a stable distribution that gradually increases from the inlet toward the deeper interior. It should be noted that the initial temperature of 42 °C at the origin (0 m) in Figure 4 represents the localized high-temperature zone in the corner/recirculation area near the heading face, where ventilation cooling is less effective, rather than the supply air temperature from the duct. At 50 m from the air duct, the temperature stabilizes at 25.7 °C, and the thermal equilibrium is maintained jointly by heat dissipation from the surrounding rock and weak convection of the airflow. The steepest temperature gradient is maintained downstream of the jet core zone, confirming that high-velocity airflow is the key driving force for improving the thermal environment.

In summary, the evolution of the roadway temperature field is the result of the combined effects of forced convection, heat conduction, and initial thermal conditions. The spatial distribution is controlled by the airflow velocity field, exhibiting axial dominance and lateral non-uniformity. Temporally, it is characterized by two stages: rapid cooling in the early stage and gradual stabilization in the later stage.

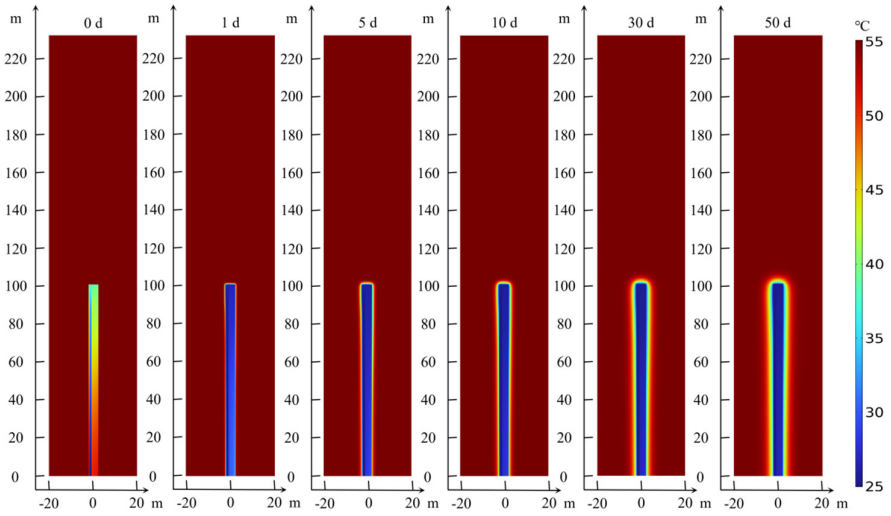

Figure 3. Temperature evolution cloud map of the roadway over time.

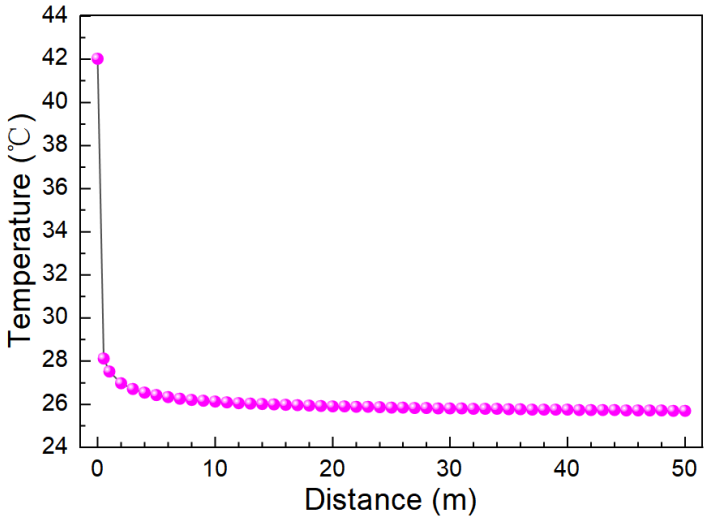

Figure 4. Curve of temperature variation along the roadway.

3.1.3. Humidity Variation Characteristics Along the Roadway

Based on the multi-field coupled numerical simulation, the evolution of the roadway humidity field is a dynamic equilibrium process governed by the combined effects of ventilation driving force, moisture dissipation from the surrounding rock, and artificial moisture sources.

It can be seen in Figure 5, at the initial moment (0 d), the system humidity is uniformly distributed, with the relative humidity stabilized at the original rock humidity of 0.7. Upon ventilation initiation, the injection of dry airflow (inlet humidity 0.6) rapidly breaks this equilibrium, forming a low-humidity zone (< 0.65) that expands axially. The heading face area, subjected to the impact of the high-velocity jet, becomes the driest zone with a relative humidity below 0.6, indicating that ventilation dominates dehumidification in the early stage. The humidity curve along the roadway also shows a steep decline within the range of 0 5 m, confirming that ventilation is the dominant factor in early-stage dehumidification. During this stage, the natural moisture dissipation from the surrounding rock is suppressed by the intense convective drying.

As ventilation continues (from initiation to 30 d), the roadway humidity field exhibits a "recovery redistribution" characteristic. The cloud maps show that the humidity in the heading face area and its adjacent regions, which had the lowest relative humidity initially, gradually recovers from below 0.6 to above 0.65. The humidity curve along the roadway exhibits a trend of "initially increasing and then decreasing." This phenomenon indicates that, on the basis of continuous moisture dissipation from the surrounding rock, water inflow and spray dust suppression continuously supply moisture to the airflow and increase its absolute humidity. However, under continuous ventilation the moisture is carried away, and the higher air temperature increases the air's moisture-holding capacity, so the relative humidity does not increase proportionally to the absolute humidity. The recovery of relative humidity in the heading face area therefore reflects the combined effect of moisture supply and ventilation removal, rather than an increase in absolute humidity alone.

After long-term ventilation (30 d to 50 d), the humidity field tends toward a dynamic equilibrium, forming a stable distribution that gradually increases from the air duct outlet toward the deeper interior. The humidity in the heading face area stabilizes within the range of 0.62 0.65. The along-roadway curves also tend to be gentle, indicating that the

rates of moisture evaporation (or condensation) and convective transport at each location have essentially reached equilibrium.

The roadway humidity evolution is a non-monotonic dynamic process: as seen in Figure 6, in the early stage, rapid drying occurs under the effect of ventilation convection; in the middle stage, relative humidity recovers and redistributes under the combined influence of surrounding rock moisture dissipation, water inflow, spray dust suppression and ventilation; in the later stage, a dynamic equilibrium is gradually achieved, jointly controlled by moisture supply, ventilation removal and air temperature. This finding indicates that ventilation and moisture supply jointly control the relative humidity field. Enhancing ventilation alone may not achieve long-term dehumidification when water inflow and spray continuously supply moisture; coordinated control of ventilation, water inflow and spray is therefore required. These recommendations follow from the modeled processes of moisture supply, ventilation removal and temperature-dependent moisture-holding capacity.

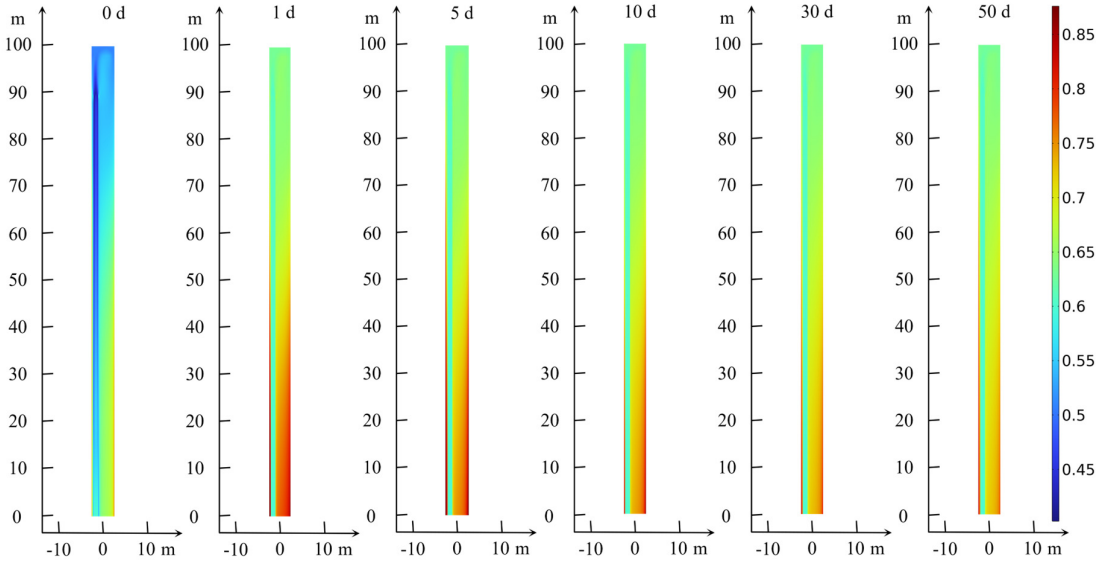

Figure 5. Humidity evolution cloud map of the roadway over time.

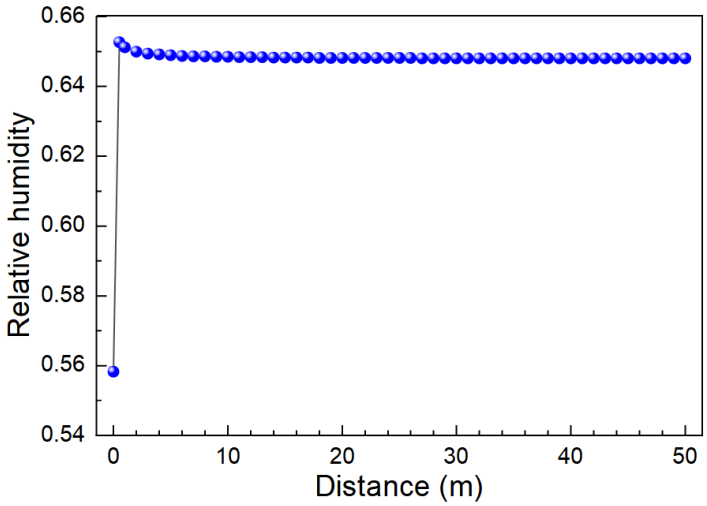

Figure 6. Curve of humidity variation along the roadway.

3.1.4. Effect of Thermal Conductivity of Surrounding Rock on Temperature and Humidity

The thermal conductivity of the surrounding rock (λ_r) is a key parameter controlling the temperature field distribution and cooling efficiency of the roadway. A comparative analysis was conducted under three operating conditions with λ_r values of 1, 2.5, and 4 W/(m·K), respectively.

As shown in Figure 7, when the thermal conductivity (λ) increases from 1 to 4 W/(m·K), the spatial distribution of the low-temperature zone exhibits a slight morphological variation. However, the overall air temperature variation across the roadway is less than 1 °C. This indicates that while thermal conductivity influences the local heat conduction gradient, its impact on the bulk air temperature is limited under the current ventilation conditions.

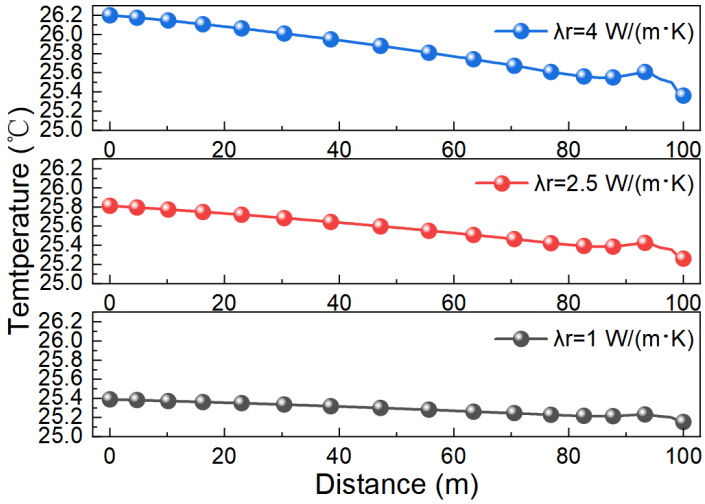

Figure 7. Temperature variation curves for surrounding rocks with different thermal conductivities.

As shown in Figure 8, by comparing the steady-state humidity cloud maps and along-roadway variation curves under λ_r values of 1, 2.5, and 4 W/(m·K), it can be seen that although higher thermal conductivity is unfavorable for roadway cooling, it increases the surface temperature of the surrounding rock, enhances the moisture evaporation capacity, and raises the saturated water vapor pressure of the air, thereby reducing the relative humidity level in the roadway.

When λ_r = 1 W/(m·K), the low-humidity zone in the roadway (relative humidity < 0.64) is relatively small, mainly concentrated near the jet core zone of the air duct. The contours of equal humidity are densely distributed across the cross-section, with a relatively large humidity gradient in the near-coal-wall region, indicating a sharp transition from the dry core to the moist boundary. As λ_r increases to 2.5 W/(m·K), the low-humidity zone expands significantly along both the axial and radial directions, and the humidity contours become gradually sparser. When λ_r reaches 4 W/(m·K), the low-humidity zone reaches its maximum extent, essentially covering most of the front half of the roadway and forming a relatively distinct dry belt, with the overall roadway humidity decreasing and the spatial distribution becoming more uniform.

From a mechanistic perspective, the thermal conductivity determines the efficiency of heat transfer from the surrounding rock interior to the roadway wall surface. The higher the thermal conductivity, the more sufficient the geothermal heat transfer to the wall surface, leading to a higher wall temperature, which in turn accelerates the evaporation of moisture contained in the surrounding rock as well as free water from water inflow

and spray. Although evaporation increases the absolute humidity in the airflow, under continuous ventilation, the moisture is promptly carried away, and the higher temperature enhances the air's capacity to hold water vapor, thereby manifesting as a reduction in relative humidity. This result indicates that the thermal conductivity of the surrounding rock not only affects the roadway temperature field but also significantly regulates the humidity field distribution through the thermal moisture coupling effect.

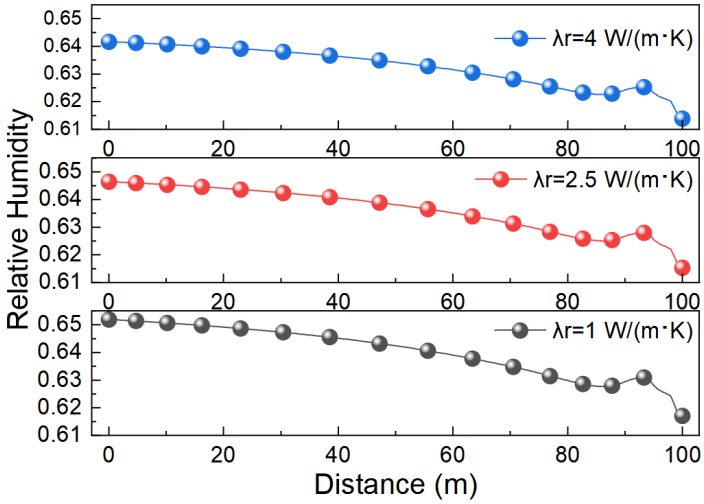

Figure 8. Humidity variation curves for surrounding rocks with different thermal conductivities.

3.1.5. Effect of Moisture Transport Coefficient of Surrounding Rock on Temperature and Humidity

The moisture transport coefficient of the surrounding rock (β) has a weak effect on the spatial distribution of the steady-state temperature field in the roadway. The moisture transport coefficient β is set within the range of 10^{-5} to 10^{-7} m^2/s. Due to the lack of direct experimental data for this specific roadway, this range was determined based on the measured and validated thermo-hydro parameters of similar deep high-temperature sandstones/rocks reported in previous studies [33]. As seen in Figure 9. When β varies within the range of 10^{-5} to 10^{-7}, the temperature curves along the entire roadway length (0–100 m) are essentially coincident, quantitatively confirming that the moisture transport coefficient is not a key parameter controlling temperature distribution. Unlike the thermal conductivity of the surrounding rock, which directly dominates sensible heat transfer, the moisture transport coefficient only affects the latent heat transfer sub-process, which accounts for a relatively small proportion in this simulation. When the effects of dominant mechanisms such as convection and conduction are significant, variations in secondary parameters are unlikely to leave a noticeable imprint on the macroscopic temperature field.

The moisture transport coefficient governs the migration process of pore water in the surrounding rock, and its cooling effect relies on the latent heat exchange (evaporative cooling) generated by moisture transport to the surface and subsequent evaporation. Under the present simulation conditions, the amount of latent heat exchange resulting from moisture migration within the surrounding rock to the surface evaporation is far smaller than the sensible heat removed by forced convection of the airflow, accounting for only a very small proportion of the overall heat exchange.

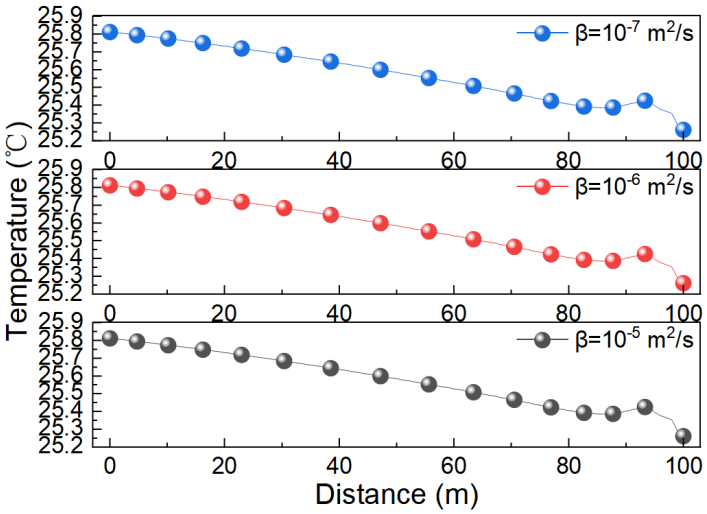

Figure 9. Temperature variation curves for different moisture transport coefficients.

The moisture transport coefficient (β) describes the migration capacity of moisture within the surrounding rock. The smaller its value, the greater the resistance and the slower the rate of moisture transport from the interior of the surrounding rock to the roadway surface.

The moisture evaporated at the roadway surface originates from the initial water-bearing layer and continuous internal replenishment. Under steady-state ventilation, internal replenishment becomes the primary moisture source. Under long-term steady-state ventilation, internal replenishment becomes the main water source for sustained evaporation. As shown in Figure 10, when β is low (e.g., 1×10^{-7} m²/s), the internal moisture replenishment is severely insufficient, resulting in a reduction in the surface evaporation source and a significant decrease in the mass of water vapor (absolute humidity) entering the airflow.

The moisture transport coefficient of the surrounding rock directly affects the humidity level by regulating the transport rate of deep moisture to the evaporation interface. The smaller the β value, the greater the resistance to internal moisture replenishment, and the weaker the evaporation intensity at the surrounding rock surface, leading to a reduction in absolute humidity in the airflow. Under conditions where the temperature field remains stable, this ultimately manifests as a significant decrease in the relative humidity of the roadway. For rock strata with the same initial humidity, differences in internal permeability or capillary water transport capacity (reflected by different β values) directly determine the wet or dry state of the working environment. A small β value results in a dry environment, whereas a large β value leads to a humid condition.

Engineering applications indicate that in working faces in low-permeability rock strata, priority should be given to cooling measures, whereas in high-permeability water-rich rock strata, it is essential to cut off the internal moisture replenishment pathways through water isolation or drainage measures to achieve effective humidity control.

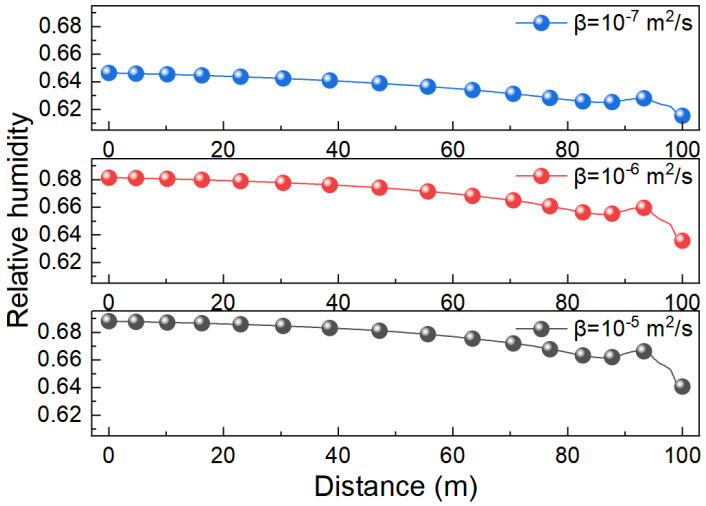

Figure 10. Roadway humidity variation curves for different surrounding rock moisture transport coefficients.

3.2. Mechanism Study of Key Physical Property Parameters on Heat Moisture Transport

3.2.1. Sensitivity Analysis Method

To quantify the influence of various factors on the temperature field of the surrounding rock, sensitivity analysis was employed to identify key parameters, and response surface experimental design was conducted using Minitab software (Version 2022). This model reveals the nonlinear mapping relationship between parameters and roadway temperature, providing a theoretical basis for thermal insulation and cooling engineering.

First, the system model for the roadway wall temperature as a function of various factors is assumed as $y = f(x_1,x_2,x_6)$, where y is the roadway wall temperature and x_i is the i-th influencing factor of the model. In the sensitivity analysis, the remaining parameters are kept at their baseline values while x_i is varied within its range. The system characteristic value y is then given by Equation (11):

$$y = f(x_{ik}, x_{ik}, \cdots, x_{ik}) \tag{11}$$

If a small change in an influencing factor causes a large change in the wall temperature, the sensitivity of the wall temperature to that factor is high, and vice versa. For ease of comparison, dimensionless processing is applied to obtain the sensitivity factor, as shown in Equation (12):

$$S_i = \left| \frac{x_i^*}{y^*} \times \frac{\Delta y}{\Delta x_i} \right| \tag{12}$$

where S_i is the sensitivity of the i-th influencing factor; x_i^* is the baseline parameter value of the i-th influencing factor; $y^*$is the system characteristic value corresponding to the baseline parameter set of the wall temperature; and $\Delta y/\Delta x$ is the rate of change in the wall temperature y with respect to the influencing factor x_i over its variation range.

The sensitivity of the wall temperature to each factor can be obtained from Equation (13), followed by factor normalization:

$$S_{i'} = \frac{S_i}{S_1 + S_2 + S_3 + S_4 + S_5 + S_6} \tag{13}$$

3.2.2. Response Surface Experimental Design

To establish the relationship between the steady-state average temperature (Y) and various factors, the response surface methodology was adopted. Using Minitab software and the Box–Behnken design, seven key factors were selected: initial rock temperature (A), heat dissipation from electromechanical equipment (B), transport heat dissipation (C), water inflow moisture (D), surrounding rock humidity (E), personnel heat dissipation (F), and spray humidification (G). Each factor was set at three levels. The established numerical model was then used to perform numerical calculations for the above, as shown in Table 2.

Table 2. Three-level value settings for each factor.

Level	Initial Rock Temperature/°C	Equipment Heat Dissipation/kW	Transport Heat Dissipation/kW	Water Inflow Moisture/(L·s^{-1})	Surrounding Rock Humidity	Personnel Heat Dissipation/kW	Spray Humidification/(L·min^{-1})
1	30	100	20	1	0.4	4	1
2	60	140	30	5	0.6	8	5
3	90	180	40	9	0.8	12	9

3.2.3. Evaluation and Analysis of the Response Surface Model

After the response surface experimental design was established, to verify the reliability of the model, a significance F-test and analysis of variance (ANOVA) were conducted on the model. The results are shown in Table 3.

Table 3. Analysis of variance for the model.

Source	DF	Adj SS	Adj MS	F-Value	*p*-Value
Model	9	521.46	57.94	118.06	0.000
A	1	8.561	8.56	17.44	0.001
B	1	3.321	3.321	6.77	0.019
C	1	6.185	6.185	12.60	0.002
D	1	4.389	4.389	8.94	0.008
E	1	12.745	12.744	25.97	0.000
F	1	0.001	0.001	0.00	0.960
G	1	0.160	0.159	0.33	0.576
AB	1	0.423	0.423	0.86	0.366
BG	1	0.003	0.003	0.01	0.936
Error	17	8.343	0.491	-	-
Total	26	529.803	-	-	-

The model passed the significance test with $p < 0.05$, indicating statistical significance. At $p < 0.05$, the significant linear terms are A (initial rock temperature), B (equipment heat dissipation), D (water inflow moisture), F (personnel heat dissipation) and G (spray humidification), and the significant two-way interactions are AB and BG. The linear terms C (transport heat dissipation) and E (surrounding rock humidity) are not significant, and all square terms and the remaining interactions are not significant. This is consistent with the ANOVA in Table 4. This indicates that within the experimental range, the relationships between the factors and the average temperature are predominantly linear and interactive, without obvious nonlinear curvature characteristics.

Under high initial rock temperature conditions, the contribution of electromechanical equipment heat dissipation to roadway temperature rise is significantly enhanced, with geothermal hazards and equipment heat generation forming a synergistic deterioration effect. Spray humidification exerts a significant inhibitory effect on the temperature rise

caused by electromechanical equipment heat dissipation. When equipment heat dissipation is large, increasing the spray rate can effectively mitigate temperature rise, providing engineering guidance for heat hazard management in mines.

Table 4. Summary of response surface models.

S	R-sq	R-sq (Adjustment)	R-sq (Prediction)
0.7	98.4%	97.6%	96.3%

The regression equation is as follows:

$$Y = 6.65 + 0.3968\ A + 0.0839\ B + 0.0927\ C - 3.9\ D - 0.2104\ E + 0.09\ F - 0.0235\ G - 0.0006\ A \times B + 0.0001\ B \times G$$

From the residual plot for average temperature in Figure 11, it can be seen that the regression model basically satisfies the assumptions of normality, homogeneity of variance, and independence, demonstrating its rationality for statistical analysis and predictive applications. The normal probability plot and histogram show that the residuals are approximately normally distributed overall, but with slight deviations at the tails, indicating some prediction errors for individual operating conditions. No obvious patterns are observed between the residuals and fitted values or observation order, suggesting that the model variance is relatively stable and the data independence is satisfactory. In summary, the model fitting effect is reasonable; however, attention should still be paid to observation points with larger residuals to further improve prediction accuracy.

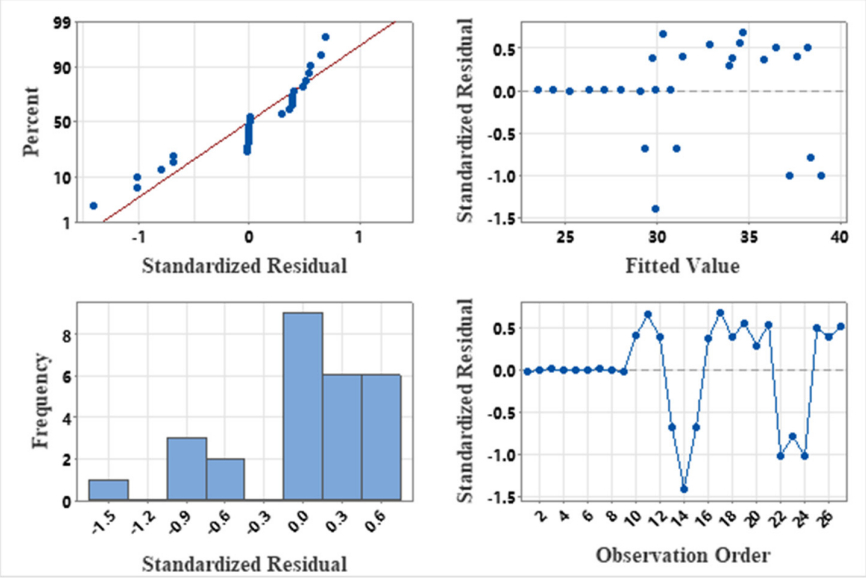

Figure 11. Residual plot for average temperature.

Based on the Pareto chart analysis of standardized effects in Figure 12, the key driving factors affecting the average temperature can be visually identified. At a significance level of $\alpha = 0.05$, the critical threshold is 2.110. Factor A (initial rock temperature) and Factor E (water inflow evaporation) are the most dominant variables, with effect values of approximately 5.1 and 4.9, respectively, significantly exceeding the critical threshold. These are followed by Factor C (transportation heat dissipation), Factor D (surrounding rock humidity), and Factor B (equipment heat dissipation), all of which also exhibit statistically significant main effects. Notably, none of the interaction terms (including AB and BG) exceed the threshold, indicating that their synergistic effects on the average temperature are statistically insignificant within the investigated range. Furthermore, the main

effects of Factor F (spray humidification) and Factor G (personnel heat dissipation) are also below the significance level.

This result corroborates the normal probability plot of standardized effects, further confirming that the initial rock temperature is the primary controlling variable for regulating the average temperature, while the interaction between equipment heat dissipation and spray humidification is also one of the key mechanisms.

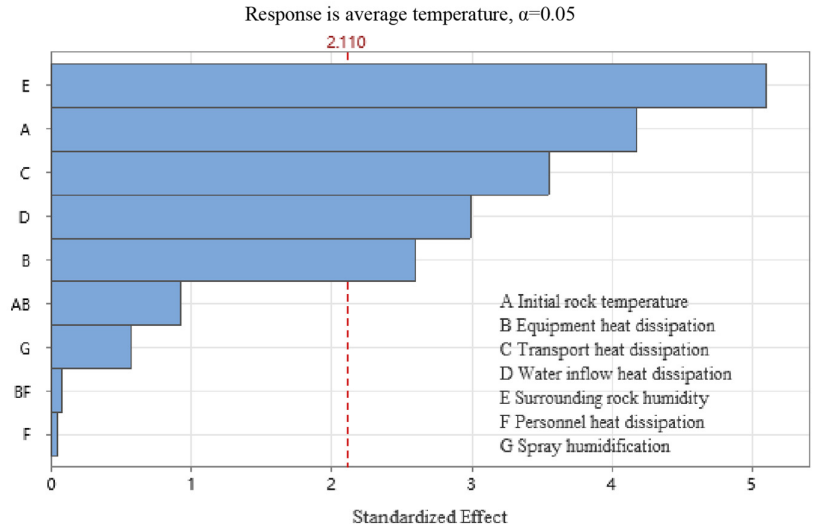

Figure 12. Pareto chart for standardized effects.

4. Discussion

The simulation results presented above reveal that coupled heat and moisture transport in the surrounding rock of deep high temperature roadways is governed by a complex interplay of multiple physical fields rather than a single dominant process. A synthesis of the parametric sensitivity analysis and the dynamic field characteristics indicates that the overall thermal and moisture response is governed by the relative magnitudes of key controlling factors, specifically the intrinsic thermal conductivity, moisture transport coefficient, and the stress-sensitive permeability. Variations in these physical parameters determine the distribution of thermal and hydraulic gradients, which in turn drive the coupled system to exhibit distinct behavioral modes over time and space. Recognizing this diversity is essential for interpreting the wide range of environmental conditions observed in practice and for designing targeted mitigation strategies.

The predicted effects are broadly consistent with previous studies, while also adding quantitative source-term information. The dominant role of rock thermal conductivity in the long-term temperature field agrees with studies on heat dissipation in high-temperature roadways, which identified thermal conductivity as a key controlling factor and showed that reducing it lowers the heat exchange intensity between the rock and the airflow [23,24]. The present simulation shows the same direction of response: increasing thermal conductivity from 1 to 4 W/(m·K) shrinks the low-temperature zone and raises the steady-state temperature at a fixed distance from the air duct.

The weak temperature sensitivity to the moisture transport coefficient β is consistent with the distinction between the moisture diffusion radius and the cooling radius in wet airways [26]. Because the diffusion radius is smaller than the cooling radius, latent heat from moisture transfer becomes significant mainly when moisture reaches the evaporation interface. In the present model, β mainly regulates moisture replenishment to the wall; when β decreases from 10^{-5} to 10^{-7} m²/s, relative humidity drops while the temperature

curves remain nearly coincident. This supports the interpretation that β affects the latent-heat sub-process rather than the dominant sensible-heat exchange under forced ventilation.

The dominant role of initial rock temperature in the response-surface analysis also agrees with multi-factor orthogonal studies, which ranked surrounding rock temperature as the most influential factor on ambient temperature [29]. The present Box–Behnken result—initial rock temperature with the largest standardized effect—falls within this range, while the significant AB and BG interactions add a source-term dimension not captured by single-factor rankings. The BG interaction indicates that the temperature penalty of equipment heat dissipation can be partially offset by spray humidification, complementing studies that identified equipment heat as a primary cause of temperature rise [31].

Finally, the ventilation-controlled non-uniform zoning predicted here is consistent with transient cooling studies of deep roadways, which showed that the effective cooling distance evolves over time and is constrained by the roadway flow structure [15,30]. The air-duct jet in the present model produces comparable axial dominance and lateral non-uniformity, supporting the view that ventilation configuration, not only rock thermal properties, should be treated as a first-order design variable in heat-hazard prediction.

The deterministic simulations in this study can be complemented by recent data-driven monitoring and digital-twin approaches. Deng et al. [34] demonstrated vision-based measurement under low-visibility harsh construction environments, which is relevant to field data acquisition in dusty and steamy roadways where optical sensing is difficult. Sharafat et al. [35] developed an interoperable digital-twin framework integrating geological, structural and operational data for TBM cutterhead design. Although developed for a different engineering object, it illustrates how heterogeneous data can support closed-loop feedback. A comparable digital twin could integrate the present heat–moisture–airflow model with real-time roadway sensor data for model calibration and adaptive ventilation/spray control.

Future research will focus on calibrating deep underground numerical models with field-monitored data to improve predictive accuracy. In this context, the application of digital twin-based multi-scale frameworks for deep underground caverns offers a promising direction for real-time thermal and moisture integrity assessment [36]. Furthermore, accurately capturing the dynamic evolution of seepage-driven water inflow [37] will be crucial for refining moisture source models in such complex environments.

5. Conclusions

This study conducted theoretical modeling, numerical simulation and parameter sensitivity analysis of coupled heat–moisture–airflow transport in the surrounding rock of deep high-temperature excavation faces. The model resolves the airflow field, the temperature field and the moisture field. The conclusions below are limited to mechanisms directly supported by the simulation results.

(1) Heat and moisture transport in surrounding rock shows clear dynamic and unsteady behavior. After roadway excavation, the temperature and humidity fields respond quickly and redistribute. Changes are intense in the early stage and gradually approach dynamic equilibrium later. Numerical simulation shows that near the air inlet, temperature drops by more than 20 °C within 1 to 5 days. After 50 days of ventilation, most of the roadway is below 35 °C. Near the heading face, relative humidity decreases from 0.7 to below 0.6, then recovers and stabilizes between 0.62 and 0.65.

(2) The thermal conductivity and moisture transport coefficient of the surrounding rock are critical parameters controlling the working face environment. A higher thermal conductivity significantly enhances heat conduction from the deep rock, causing a

sharper rise in airflow temperature and shrinking the low-temperature zone. Conversely, a lower moisture transport coefficient hinders internal moisture migration to the evaporation interface, reducing relative humidity. Response surface analysis further reveals that initial rock temperature and equipment heat dissipation are the most dominant factors, with a clear interaction between equipment heat dissipation and spray humidification.

(3) Parameter sensitivity analysis shows that initial rock temperature and equipment heat dissipation are the most important factors affecting working face air temperature. Equipment heat dissipation and spray humidification have a clear interaction, which provides a basis for coordinated optimization of cooling strategies. The consistency between simulation results and theoretical mechanisms shows that the multifield coupling model and analytical method can effectively reveal the formation and evolution of the heat and moisture environment in deep excavation faces. This has theoretical value for heat hazard prevention and ventilation design in mines.

Author Contributions: Conceptualization, Y.S.; methodology, J.L.; software, J.L.; validation, K.W.; formal analysis, J.L.; investigation, Y.L.; resources, S.M.; data curation, Y.L.; writing—original draft preparation, Y.L.; writing—review and editing, J.L.; visualization, Y.L.; supervision, Y.S.; project administration, Y.L.; funding acquisition, Y.S. All authors have read and agreed to the published version of the manuscript.

Funding: This research was funded by The Key Research and Development Program of Shaanxi (Program No. 2024PT ZCK 70).

Institutional Review Board Statement: Not applicable.

Informed Consent Statement: Not applicable.

Data Availability Statement: The data presented in this study are available on request from the corresponding author.

Conflicts of Interest: Yanzi Lei, Yuliang Sun, Kaipeng Wang and Shaoming Ma are affiliated with CCTEG Xi'an Research Institute (Group) Co., Ltd. and with Xi'an Coal Science Geothermal Energy Development Co., Ltd. The remaining authors declare that the research was conducted in the absence of any commercial or financial relationships that could be construed as a potential conflict of interest.

References

1. Xie, H.P. Research review of the state key research development program of China: Deep rock mechanics and mining theory. *J. China Coal Soc.* **2019**, *5*, 1283–1305. https://doi.org/10.13225/j.cnki.jccs.2019.6038
2. Xie, H.P.; Zhou, H.W.; Xue, D.J.; Wang, H.W.; Zhang, R.; Gao, F. Research and consideration on deep coal mining and critical mining depth. *J. China Coal Soc.* **2012**, *37*, 535–542. https://doi.org/10.1007/s11783-011-0280-z
3. Kang, H.P.; Wang, G.F.; Jiang, P.F.; Wang, J.C.; Zhang, N.; Jing, H.W.; Huang, B.X.; Yang, B.G.; Guan, X.M.; Wang, Z.G. Conception for strata control and intelligent mining technology in deep coal mines with depth more than 1000 m. *J. China Coal Soc.* **2018**, *43*, 1789–1800. https://doi.org/10.13225/j.cnki.jccs.2018.0634
4. Zhang, X.; Wu, Z. Spatiotemporal Evolution of Energy Consumption Carbon Emissions and Regional Low Carbon Sustainable Development in China. *Sustainability* **2026**, *18*, 7157. https://doi.org/10.3390/su18147157.
5. Song, J.K.; Yuan, Y.M.; Liu, X.Y.; Ma, Z.; Wang, J.N.; Yan, Z.W. Multiphysics collaborative detection technology and equipment development in deep earth engineering: Challenges, advances, and future trends. *Appl. Geophys.* **2026**, *23*, 814–842. https://doi.org/10.1007/s11770-025-1338-1.
6. Yuan, L.; Zhang, P. Development status and prospect of geological guarantee technology for precise coal mining. *J. China Coal Soc.* **2019**, *44*, 2277–2284. https://doi.org/10.13225/j.cnki.jccs.KJ19.0571
7. Yuan, L.; Zhang, T.; Wang, Y.; Wang, X.; Wang, Y. Scientific problems and key technologies for safe and efficient mining of deep coal resources. *J. China Coal Soc.* **2025**, *50*, 1–12. https://doi.org/10.13225/j.cnki.jccs.YG25.0016

8. Yuan, L. Research progress of mining response and disaster prevention and control in deep coal mines. *J. China Coal Soc.* **2021**, *46*, 716–725. https://doi.org/10.13225/j.cnki.jccs.YT21.0158
9. Qin, B.; Ma, D. Research progress and challenges in prevention and control of combined disasters of coal spontaneous combustion and methane in coal mine goaf. *J. China Coal Soc.* **2025**, *50*, 392–408. https://doi.org/10.13225/j.cnki.jccs.ST23.1624
10. Wang, H.; Qin, Y.; Tang, F.; Sun, J. Bibliometric review of mine thermal environment research based on knowledge graph analysis: Evolution, trends, and future directions. *J. Therm. Anal. Calorim.* **2026**, *151*, 125–141. https://doi.org/10.1007/s10973-025-15182-9.
11. You, B.; Chen, Y.; Yang, M.; Gao, K.; Cui, D.; Lu, M. Management of thermal hazards in deep mines in China: Applications and prospects of mine cooling technology. *Water* **2024**, *16*, 2347. https://doi.org/10.3390/w16162347.
12. Cheng, L.; Yan, S.; Zhou, X.; An, Z.; Qu, X.; Li, X. Towards Sustainable Deep Mining: A Knowledge Graph Based Critical Review of Deep Mine Cooling and Heat Hazard Management. *Sustainability* **2026**, *18*, 6393. https://doi.org/10.3390/su18136393.
13. Hao, J.; Liang, B.; Sun, W. Analysis of Thermo-Hydro-Mechanical Coupling of Coal and Gas With Absorption/Desorption Thermal Effect. *Shock Vib.* **2020**, *2020*, 6674107. https://doi.org/10.1155/2020/6674107.
14. Wu, D.; Li, B.; Wu, J.; Hu, G.; Gao, X.; Lu, J. Influence of mineral composition on rock mechanics properties and brittleness evaluation of surrounding rocks in soft coal seams. *ACS Omega* **2024**, *9*, 1375–1388. https://doi.org/10.1021/acsomega.3c07731.
15. Wang, C.; Lin, Q.; Lang, X.; Xu, Y.; Wang, X.; Fan, Y. Prediction of temperature field and control method for heat damage in deep shaft. *Geofluids* **2025**, *2025*, 5553346.
16. He, M.C. Application of HEMS cooling technology in deep mine heat hazard control. *Min. Sci. Technol.* **2009**, *19*, 269–275. https://doi.org/10.1016/s1674-5264(09)60051-x.
17. Li, Z.; Xu, Y.; Li, R.; Jia, M.; Wang, Q.; Chen, Y.; Cai, R.; Han, Z. Impact of the water evaporation on the heat and moisture transfer in a high temperature underground roadway. *Case Stud. Therm. Eng.* **2021**, *28*, 101551. https://doi.org/10.1016/j.csite.2021.101551.
18. Zhen, Z.; Yu, K.; Wan, Z.; Ju, Y.; Yu, Z.; Jiang, L.; Wang, Z.; Zhang, B.; Shi, P.; Sun, Z. Assessing and utilizing hydrothermal geothermal resources in a deep mine: A case study of Pingdingshan coalfield, China. *Bull. Eng. Geol. Environ.* **2026**, *85*, 595. https://doi.org/10.1007/s10064-026-05260-z.
19. Xu, Y.; Chen, L.; Zhang, J.; Ji, H. Research progress of heat damage prevention and control technology in deep mine. *Sustainability* **2025**, *17*, 6200. https://doi.org/10.3390/su17136200.
20. Qin, Y.; Sun, J.; Wang, C.; Ren, Z.; Li, Y.; Wang, H.; Xu, Y. Similarity simulation study on coal mine goaf temperature field dynamic evolution influenced by initial stop mining temperature. *Case Stud. Therm. Eng.* **2026**, *79*, 107748. https://doi.org/10.1016/j.csite.2026.107748.
21. Qin, Y.; Guo, M.; Tang, F.; Liu, Q.; Zhang, J.; Hou, H.; Zhao, W. Numerical simulation of temperature field in surrounding rock of coal mining face based on cyclic advancement algorithm. *J. China Coal Soc.* **2025**, *50*, 409–420. https://doi.org/10.13225/j.cnki.jccs.2024.0046
22. Qu, M.; Fan, W.; Chen, X.; Mu, H.; Tan, Q.; Shao, B.; Zhang, Y. Law of the damp heat in mines and its application exploration based on FST. *J. Therm. Anal. Calorim.* **2024**, *149*, 5903–5917. https://doi.org/10.1007/s10973-024-13069-9.
23. Wang, H. Numerical study of surrounding rock heat dissipation and wind temperature prediction in high geotemperature coal face. *Energy Explor. Exploit.* **2024**, *42*, 17–39. https://doi.org/10.1177/01445987231187658.
24. Tang, F.; Qin, Y.; Guo, M.; Wang, S.; Wang, P.; Yang, Y. Research on temperature field and heat dissipation development regularity of surrounding rock in adjacent parallel roadway: Simulation and similar experiment. *Case Stud. Therm. Eng.* **2025**, *73*, 106706. https://doi.org/10.1016/j.csite.2025.106706.
25. Mu, D.; Zhang, K.; Ma, Q.; Wang, J. A coupled hydro thermo mechanical model based on TLF-SPH for simulating crack propagation in fractured rock mass. *Geomech. Geophys. Geo Energy Geo Resour.* **2024**, *10*, 33. https://doi.org/10.1007/s40948-024-00756-y.
26. Wang, Y.J.; Zhou, G.Q.; Wu, L. Unsteady heat moisture transfer of wet airway in deep mining. *J. Cent. South Univ.* **2013**, *20*, 1971–1977. https://doi.org/10.1007/s11771-013-1697-2.
27. Zhang, Y.; Wang, L. A coupled thermo hydro mechanical lattice Boltzmann–Peridynamic model for rock masses fracturing. *Comput. Geotech.* **2026**, *190*, 107749. https://doi.org/10.1016/j.compgeo.2025.107749.
28. Li, B.; Xu, H.; Song, Y.J.; Zhang, H.L.; Wang, W.W.; Zhao, F.Y. Heat and moisture transports in a slot ventilated enclosure packed with discrete porous media: Mixing convection instability, oscillation and resonance. *Int. J. Therm. Sci.* **2023**, *194*, 108603. https://doi.org/10.1016/j.ijthermalsci.2023.108603.

29. Qin, Y.; Wang, S.; Tang, F.; Wang, P.; Guo, M.; Yang, Y. Research on temperature field of dimensionless surrounding rock at excavation roadway based on finite volume method. *J. China Coal Soc.* **2026**, *51*, 3458–3469. https://doi.org/10.13225/j.cnki.jccs.2025.0503
30. Xue, P.; You, S.; Chao, J.; Ye, T. Numerical investigation of unsteady airflow in subway influenced by piston effect based on dynamic mesh. *Tunn. Undergr. Space Technol.* **2014**, *40*, 174–181. https://doi.org/10.1016/j.tust.2013.10.004.
31. Wang, X.; Chen, X.; Ma, H.; Li, S.; Song, X. Numerical analysis and performance evaluation of cooling system in coal mining face: A comprehensive study on thermal and humidity characteristics. *Therm. Sci. Eng. Prog.* **2024**, *47*, 102288. https://doi.org/10.1016/j.tsep.2023.102288.
32. Su, P. Thermal Environment Simulation and Safety Prewarning of Hot Mines Based on Big Data. *Int. J. Heat Technol.* **2022**, *40*, 63–70. https://doi.org/10.18280/ijht.400108.
33. Li, J.; Lei, Y.; Li, L.; Chen, S. Heat transfer performance analysis of medium–deep coaxial borehole heat exchanger: combination of heat extraction operation test and numerical simulation. *J. Therm. Sci. Eng. Appl.* **2025**, *17*, 011004. https://doi.org/10.1115/1.4066600.
34. Deng, T.; Sharafat, A.; Lee, S.; Seo, J. Automatic vision-based dump truck productivity measurement based on deep-learning illumination enhancement for low-visibility harsh construction environment. *J. Constr. Eng. Manag.* **2024**, *150*, 04024154. https://doi.org/10.1061/jcemd4.coeng-14194.
35. Sharafat, A.; Tanoli, W.A.; Yoo, S.; Seo, J. Digital twin framework for cutterhead design and assembly process simulation optimization for TBM. *Appl. Sci.* **2026**, *16*, 1865. https://doi.org/10.3390/app16041865.
36. Sharafat, A.; Tanoli, W.A. Digital twin–based multi-scale framework for seismic integrity assessment of deep underground caverns. *Sci. Rep*. **2026**, *16*, 25599. https://doi.org/10.1038/s41598-026-55412-0.
37. Tanoli, W.A.; Sharafat, A. Seepage Analysis and Piping Control for the Soft-Ground Stretch of a Hydropower Headrace Tunnel Adjacent to a Valley Slope. *Appl. Sci.* **2026**, *16*, 10625. https://doi.org/10.3390/app162110625.

Disclaimer/Publisher's Note: The statements, opinions and data contained in all publications are solely those of the individual author(s) and contributor(s) and not of MDPI and/or the editor(s). MDPI and/or the editor(s) disclaim responsibility for any injury to people or property resulting from any ideas, methods, instructions or products referred to in the content.